Quantitative Susceptibility Mapping in the Abdomen as an Imaging Biomarker of Hepatic Iron Overload

Samir D. Sharma[1,*], **Diego Hernando**[1], **Debra E. Horng**[1,2], and **Scott B. Reeder**[1,2,3,4]

[1]Department of Radiology, University of Wisconsin, Madison, Wisconsin, USA

[2]Department of Medical Physics, University of Wisconsin, Madison, Wisconsin, USA

[3]Department of Biomedical Engineering, University of Wisconsin, Madison, Wisconsin, USA

[4]Department of Medicine, University of Wisconsin, Madison, Wisconsin, USA

Abstract

Purpose—The purpose of this work was to develop and demonstrate feasibility and initial clinical validation of quantitative susceptibility mapping (QSM) in the abdomen as an imaging biomarker of hepatic iron overload.

Theory—In general, QSM is faced with the challenges of background field removal and dipole inversion. Respiratory motion, the presence of fat, and severe iron overload further complicate QSM in the abdomen. We propose a technique for QSM in the abdomen that addresses these challenges.

Methods—Data were acquired from 10 subjects without hepatic iron overload and 33 subjects with known or suspected iron overload. The proposed technique was used to estimate the susceptibility map in the abdomen, from which hepatic iron overload was measured. As a reference, spin-echo data were acquired for R2-based LIC estimation. Liver R2* was measured for correlation with liver susceptibility estimates.

Results—Correlation between susceptibility and R2-based LIC estimation was $R^2 = 0.76$ at 1.5T and $R^2 = 0.83$ at 3T. Further, high correlation between liver susceptibility and liver R2* ($R^2 = 0.94$ at 1.5T; $R^2 = 0.93$ at 3T) was observed.

Conclusion—We have developed and demonstrated initial validation of QSM in the abdomen as an imaging biomarker of hepatic iron overload.

Keywords

magnetic susceptibility; quantitative susceptibility mapping; liver iron concentration; dipole inversion; imaging biomarker

---

*Correspondence to: Samir D. Sharma, PhD, Department of Radiology, University of Wisconsin, 1122Q WIMR, 1111 Highland Ave., Madison WI 53705 sdsharma2@wisc.edu.

INTRODUCTION

Excessive accumulation of iron in the body can occur in people with hereditary hemochromatosis or in those who require repeated intravenous blood transfusions (i.e. transfusional hemosiderosis) (1,2). Excess iron in the body is toxic and can cause multiple health complications including liver and heart damage, pancreatic dysfunction, and growth failure. The body has very limited capability to remove excess iron (3), and therefore treatment is often required to reduce total body iron content. Oral chelation agents are commonly prescribed for treatment, but they are expensive (>$40,000/year) and have side effects (4,5). The ability to accurately and longitudinally assess body iron content is critical for treatment monitoring, to avoid over- or under-treatment while ensuring that safe iron levels are maintained, and to minimize side effects.

Serum markers (e.g. ferritin concentration) are commonly used to assess body iron content. Ferritin is a relatively simple and inexpensive biomarker of body iron content. However, ferritin is well known to be confounded by a number of factors (e.g. inflammation) and often does not accurately reflect total body iron content (6).

Liver iron concentration (LIC) is a reliable indicator of total body iron content (7). Therefore, measurement of LIC may serve as a surrogate for the measurement of body iron content. To this end, liver biopsy samples have been used to measure LIC. While liver biopsy enables accurate iron quantification, it is invasive, expensive, and suffers from high sampling variability (8). Further, biopsy cannot be performed in patients with thrombocytopenia or bleeding diatheses due to the risk of uncontrolled bleeding. Alternatively, biomagnetic liver susceptometry (BLS) using a superconducting quantum interference device (SQUID) is well validated for the measurement of LIC (9–11). BLS measures magnetic susceptibility, which is a fundamental property of all materials including tissue. Since iron is the only non-trace element in the liver that significantly alters susceptibility, the iron concentration can be determined by measuring the magnetic susceptibility of tissue. While BLS has been validated for measurement of LIC, its complexity and very limited availability (only four devices worldwide) have prevented its widespread use.

MRI is a widely available and safe technology with no ionizing radiation. MRI is very sensitive to the paramagnetic effects of iron on tissue susceptibility. Current MR-based methods for measuring LIC map the decay rate (e.g. R2 or R2*) of the transverse signal (12–14). These methods have demonstrated good correlation with LIC. However, empirically derived calibrations have varied amongst different research groups, which may reflect the uncertainty in the indirect relationship between the measured relaxation parameter and LIC.

Susceptibility is a fundamental property of all materials, including liver tissue. MR-based susceptibility mapping would thus enable a direct measure of iron concentration. Quantitative susceptibility mapping (QSM) techniques have been developed for quantifying iron deposits in the brain (15–17). However, these techniques have not been successfully implemented in the abdomen. Application of QSM in the abdomen is faced with several

additional technical challenges that are not problematic for QSM in the brain, including respiratory motion, the presence of fat in the abdomen, as well as the rapid signal decay in cases of severe hepatic iron overload. Previous works have approximated susceptibility mapping in the abdomen by using boundary approaches (18–20). While these approaches have demonstrated the potential for susceptibility mapping in the abdomen, they require assumptions about the object geometry, they restrict that measurements be near the tissue boundary (i.e. they do not provide susceptibility maps), and they do not account for background field variations.

Therefore, the purpose of this work was to develop and demonstrate feasibility and initial clinical validation of QSM in the abdomen as an imaging biomarker of hepatic iron overload. The proposed QSM technique is tested at both 1.5T and 3T, in ten controls without iron overload and in 33 subjects with known or suspected hepatic iron overload. We compare the liver susceptibility measurements to LIC estimates using an FDA-approved R2-based method known as Ferriscan (12). Further, we analyze the correlation between liver susceptibility and liver R2* as well as the correlation and agreement between liver susceptibility estimates at 1.5T and 3T.

THEORY

Background

The magnetic susceptibility distribution (χ) can be decomposed into local (χ_L) and background (χ_B) components, where χ_L represents the susceptibility distribution within a spatial region of interest (ROI) (e.g. tissue) while χ_B represents the susceptibility distribution outside of the ROI (21). Therefore, each spatial location of the susceptibility distribution is a component of either χ_L or χ_B, but not both.

The mathematical relationship between the susceptibility distribution and the resonance frequency shift that is caused by B_0 field inhomogeneity (i.e. B_0 field map) (ψ) can be written as (22–24):

$$\psi(\mathbf{r}) = \frac{\gamma}{2\pi} B_0 (d(\mathbf{r}) * \chi(\mathbf{r})) + N(\mathbf{r}) \quad [1]$$

where $\gamma/2\pi$ is the gyromagnetic ratio (i.e. 42.58 MHz/T for ^{1}H), B_0 is the main magnetic field strength (in T), and $d(\mathbf{r}) = \frac{3\cos^2(\theta) - 1}{4\pi|\mathbf{r}|^3}$ is the dipole response kernel (25), where θ is the angle with respect to the main magnetic field axis and $\mathbf{r}$ is the position vector, and * denotes the linear convolution operation. The noise, $N(\mathbf{r})$, is modeled as additive Gaussian with unequal variance (26). Eq. 1 can be equivalently represented in the Fourier domain as

$$\tilde{\psi}(\mathbf{k}) = \frac{\gamma}{2\pi} B_0 \left(\frac{1}{3} - \frac{k_z^2}{|\mathbf{k}|^2} \right) \tilde{\chi}(\mathbf{k}) + \tilde{N}(\mathbf{k}) \quad [2]$$

where the tilde (~) represents the Fourier domain representation of each variable, and $\mathbf{k} = [k_x, k_y, k_z]$ denotes the Fourier-space coordinates.

Like the susceptibility distribution, the B_0 field map can be decomposed into local (ψ_L) and background (ψ_B) components, where each component indicates the source of the field inhomogeneity. For example, the local field represents the field inhomogeneity that is caused by the local susceptibility distribution: $\psi_L(\mathbf{r}) = \frac{\gamma}{2\pi} B_0(d(\mathbf{r}) * \chi_L(\mathbf{r}))$. Because $d(\mathbf{r})$ is a nonlocal function, the B_0 field map value at any spatial location is composed of contributions from both the local field and the background field.

General challenges for QSM

The objective of QSM is to estimate the local susceptibility distribution (χ_L) from the measured B_0 field map (ψ). In general, QSM is faced with two challenges: 1) removal of the background field from the B_0 field, to isolate the local field, and 2) inversion of the dipole response kernel from the local field to recover the local susceptibility distribution.

Background field removal is most often performed using either the projection onto dipole fields (PDF) method (21) or the sophisticated harmonic artifact reduction for phase data (SHARP) method (17). SHARP exploits the observation that the background field (ψ_B) is a harmonic function within the ROI while the local field (ψ_L) is assumed not to be harmonic within the ROI (27). Using the mean value property of harmonic functions, the background field can be removed by solving the following expression for ψ_L:

$$WL\psi = WL\psi_L \quad [3]$$

where L represents a discrete Laplace operator and W is a weighting mask that defines the reliability of the estimate at each voxel. Because the matrix WL is singular, regularization must be incorporated into the estimation to properly recover ψ_L. Recent works have proposed using truncated singular value decomposition (17) or Tikhonov regularization (28). The removal of the background field in the abdomen may be challenging due to the air in the gut and lungs.

The dipole inversion step consists of solving the following expression for χ_L:

$$\psi_L = D\chi_L \quad [4]$$

where D represents the scale factor, $\gamma B_0/2\pi$, and the dipole response function, $d(\mathbf{r})$, in matrix form. Regularization is also required in this inversion since the dipole response function contains values equal to or close to zero (in the Fourier domain) at and near the magic angle of 54.74° (29), resulting in an ill-posed or severely ill-conditioned inverse problem. Many regularization techniques for dipole inversion have been proposed; they are generally classified as either a Fourier domain method (15,30,31), which modifies the Fourier representation of the dipole kernel, or an image domain method (16,32), which imposes spatial constraints on the estimated susceptibility map. Multiple angle methods also exist (17,33), however the current work focuses on a single angle acquisition, which is more practical in abdominal applications.

Additional challenges for QSM in the abdomen

The application of QSM in the abdomen is further complicated by challenges that are not present in brain QSM. These additional challenges include: 1) respiratory motion, 2) the presence of fat, and 3) rapid signal decay from severe iron overload.

Respiratory motion during the acquisition corrupts the source images, which in turn, will compromise the fidelity of the reconstructed B_0 field map. If unaccounted for (either prospectively or retrospectively), errors in the B_0 field map will reduce the accuracy of the estimated susceptibility map. Secondly, fat is present within the liver in up to 30% of the general population (34) as well as throughout the abdomen in the forms of subcutaneous and visceral adipose tissue. The presence of fat introduces an additional chemical species, which confounds the estimate of the B_0 field map. Fat is composed of multiple spectral peaks, each of which precesses at a different frequency than water. The presence of these fat peaks must be included in the reconstruction to ensure accurate estimation of the B_0 field map. Finally, subjects with severe hepatic iron overload may have iron concentrations in excess of 10 mg Fe/g dry tissue, as compared to the smaller concentrations of iron in the brain (< 2 mg Fe/g dry tissue) (35,36). These high liver iron concentrations result in a rapid decay of the transverse signal in the liver as well as a highly non-uniform noise variance in the reconstructed B_0 field map.

Proposed technique for abdominal QSM

In this work, we propose a technique for abdominal QSM by developing both the data acquisition and the image reconstruction in a way that addresses the challenges described above.

The source images are acquired using an accelerated breath-held sequence that effectively freezes respiratory motion throughout the data acquisition window. All images are acquired in the same breath-hold and therefore are co-registered. In addition, the pulse sequence acquires source images using a short first echo time (TE_1 = 1.2ms) and short echo spacing (2ms at 1.5T; 1ms at 3T) in order to capture the rapidly decaying signal in cases of severe iron overload.

The B_0 field map is estimated using a chemical shift encoded reconstruction (37,38). This reconstruction models the water peak and the multiple peaks of the fat spectrum (39), which were derived from a previous spectroscopic study (40). By including this spectral model in the reconstruction, the B_0 field map is inherently corrected for the presence of fat. Combining Eqs. 3 and 4, the local susceptibility distribution can be modeled directly to the B_0 field map as

$$WL\psi = WLD\chi_L \quad [5]$$

The matrix WLD is singular, and therefore χ_L cannot be estimated using a simple linear least-squares approach. To overcome the ill-posed nature of this inverse problem, we incorporate a regularization term that penalizes the edges in the estimated susceptibility distribution that do not appear in the magnitude source images (16,32). This form of

regularization exploits the observation that edges in the source images occur at the boundaries of tissues with different susceptibility values. Thus, an edge that appears in the estimated susceptibility map but not in the source images is treated as an artifact and penalized accordingly.

Although the presence of fat poses a challenge in abdominal QSM, it also offers a unique opportunity for further spatial regularization. Adipose tissue does not accumulate excess iron in patients with iron overload (41). We exploit this fact by assuming that a contiguous region of adipose tissue has a nearly uniform susceptibility. This "fat-constraint" further penalizes variations in the estimated susceptibility map that occur in regions of adipose tissue.

Using both the edge and fat constraints to regularize the inverse problem, Eq. 6 presents the expression for estimating the local susceptibility distribution from the B_0 field map.

$$\min_{\chi_L} \|WL(\psi - D\chi_L)\|_2^2 + \lambda \|WCG\chi_L\|_2^2 \quad [6]$$

In Eq. 6, *C* contains the penalty values for both the edge and fat constraints, and *G* denotes the 3D finite-difference operator. The weighting term *W* accounts for the non-uniform noise variance in the field map (26). To balance the two terms, this weighting is also included in the regularization penalty. Finally, the scalar regularization parameter (λ) determines the tradeoff between data fidelity and regularization. An l_2-regularization was used to maintain linearity of the inverse problem. This convex minimization problem can be solved using a variety of standard numerical techniques (42).

METHODS

Acquisition

Experiments were conducted after obtaining IRB approval and informed consent. Imaging was performed on a clinical 1.5T scanner (HDxt, v16.0, GE Healthcare, Waukesha, WI) using an 8-channel phased array body coil, and on a clinical 3T scanner (MR750 v22.0, GE Healthcare, Waukesha, WI) using a 32-channel phased array body coil (Neocoil, Pewaukee, WI), of which the upper 20 elements were used. Only the upper 20 elements of the 32-channel body coil were used because the remaining 12 elements were inferior to the abdomen, and do not improve SNR when the target imaging area is the abdomen. Data were acquired from ten control subjects with no hepatic iron overload, and from 33 subjects with known or suspected hepatic iron overload. Subjects with iron overload had either hereditary hemochromatosis or hemosiderosis, resulting from a variety of transfusion-dependent anemias, leukemia, or myelodysplastic syndrome. Each subject was scanned at both 1.5T and 3T on the same day using a 3D six-echo gradient-echo chemical shift encoded sequence. Full 3D coverage of the liver was achieved in one breath-hold of 19–22s. In addition, each subject was scanned using a 2D multi-slice spin-echo sequence at 1.5T. The spin-echo data were acquired in order to perform R2-based liver iron quantification (Ferriscan) (12). Table 1 lists the relevant parameters for each of the three acquisitions. We note that of the data used in this current study, the data from nine control subjects and 18 subjects with known or suspected hepatic iron overload were also used in a previous study that demonstrated the

feasibility of quantifying liver iron from the B_0 field map using a fat-referenced boundary approach (20). That study did not perform background field removal or the full dipole inversion. Further, the QSM reconstruction, data analysis, and statistical analysis steps performed in this current study were performed independently of the previous study.

Reconstruction

Figure 1 shows the process of reconstructing the local susceptibility map from the multi-echo gradient-echo data. A chemical shift encoded reconstruction (37,38) was used to reconstruct the B_0 field map as well as separated water and fat images and an R2* map from the source images. An initial estimate of these parameters was achieved using a 2D graphcut algorithm that was implemented slice-by-slice (38). This algorithm has been shown to be a highly robust approach for the estimation of the water and fat images as well as the B_0 field and R2* maps. However the graphcut algorithm uses a regularization term, equal to 0.02 in this work, which introduces bias (spatial smoothing) into the estimate of the B_0 field map. To remove this bias, the initial estimates from the graphcut algorithm were refined by using a voxel-wise fit without any regularization (37). Unlike in (37), we did not low-pass filter the B_0 field map; therefore, the final estimate of the B_0 field map was not smoothed. It is important to note that the chemical shift encoding reconstruction estimates the B_0 field map directly from the source images; a separate phase unwrapping step is not required.

The noise standard deviation in the B_0 field map is inversely proportional to the SNR of the magnitude images (26). We used the root-sum-of-squares (RSS) of the source images as a surrogate for the SNR. More specifically, the data weighting mask, W, was calculated as the RSS of the six echo time images (i.e. $\sqrt{\sum_{i=1}^{6} |S_i|^2}$, where $|S_i|$ is the magnitude of the ith source image), and then normalized so that the maximum value of W was equal to one. Calculating W in this manner accounts for the non-uniform noise variance in the B_0 field map. Voxels with higher SNR (i.e. lower R2* decay) are given a stronger weighting than those with lower SNR (i.e. higher R2* decay).

To generate the edge constraint, the edges were found by applying a threshold on the spatial finite-difference of the magnitude source images. Edges that represented chemical shift contrast were derived from a source image that was acquired when the water peak and the methylene peak of fat were closest to opposed-phase. At 1.5T, the fourth echo image was used (TE = 7.2ms) and at 3T, the first echo image (TE = 1.2ms) was used. The edges that represented R2* contrast were derived from the RSS image. In both cases, the threshold was chosen so that the largest 20% of the finite-differences were assumed to represent edges. The fat weighting mask was generated using a threshold value of 0.8 on the fat fraction map, which was calculated using the magnitude discrimination method (43). The composite weighting mask, C, was calculated in the following manner. First, each edge in the chemical shift contrast mask and the R2* contrast mask was copied to an intermediate composite mask. Second, the intermediate composite mask and the fat mask were summed to produce the composite mask. Figure 2 shows an example of the individual masks as well as the composite mask.

The joint background field removal and dipole inversion reconstruction (Eq. 6) was implemented using a linear conjugate gradient method (44) in Matlab (The Mathworks Inc., Natick, MA) 64-bit Linux, 4 Octo Core AMD 6134, 128 GB RAM). The total reconstruction time was approximately three hours per 3D dataset. The reconstruction has not yet been optimized for reconstruction time.

A spherical kernel with a radius equal to 6mm was used for the Laplacian (*L*) (45). The application of the dipole kernel, *D*, was performed efficiently by using a pointwise multiplication in the Fourier domain rather than a convolution in the image domain. The image domain data were zero-padded by a factor of 2 before Fourier transform to ensure linear convolution (46). The regularization parameter was determined using an L-curve analysis (47) on three of the datasets with varying degrees of hepatic iron overload. A value of $\lambda = 2\times10^{-1}$ was chosen based on the L-curve analysis and by visual inspection of the estimated susceptibility maps. Figure 3 shows an example of the estimated susceptibility maps for one of the datasets reconstructed using many values of λ. The three datasets used for the L-curve analysis were excluded from any further analysis.

Data Analysis

Because all QSM inversion algorithms provide estimates of relative (not absolute) susceptibility values, the susceptibility of the liver was measured relative to the susceptibility of the subcutaneous adipose tissue. The subcutaneous adipose tissue was used as the reference to determine susceptibility in the liver because it is does not accumulate excess iron (41). An ROI of radius ~2 cm was placed in a single slice in the right lobe of the liver away from major vessels. Another ROI was placed in the same slice in the nearby subcutaneous adipose tissue. The major radius of this ROI ranged from 1–2 cm and the minor radius ranged from 0.5–1 cm, depending on the amount of adipose tissue for each subject. The measurements were first performed in the dataset acquired at 1.5T, and then in the 3T dataset using a visual alignment of the two datasets.

It is possible to convert the susceptibility difference (i.e. $\Delta\chi = \chi_{liver} - \chi_{adipose}$) to an estimate of LIC (in mg Fe/g dry tissue). However, the conversion factor from susceptibility to LIC has not yet been fully characterized (11,35,48,49). To prevent the uncertainty in the conversion from biasing our results, we have plotted the susceptibility difference against the LIC estimate from Ferriscan (described later). Using previously proposed conversion factors, we have also calculated susceptibility-based estimates of LIC to compare with the Ferriscan-based LIC estimate.

The susceptibility-based LIC was calculated in the following way. A baseline susceptibility difference was calculated as the average of the susceptibility differences from all of the control subjects. A baseline iron concentration was also calculated as the average of the Ferriscan-LIC estimates from all of the control subjects. For the subjects with known or suspected hepatic iron overload, the susceptibility difference in excess of the baseline difference was attributed to hepatic iron overload. This susceptibility "overload" (χ_{OL}) was converted to overload iron concentration (LIC_{OL}) using three different conversion factors. First, we used a factor of 0.89 ppm/(mg/g wet), which was derived by Langkammer et al. using inductively coupled plasma mass spectrometry in the post mortem brains of 13

subjects (35). Next, we used a factor of 1.2 ppm/(mg/g wet), which was proposed by Ghugre et al. using literature values derived from horse spleen and in humans (48). Lastly, we used a factor of 1.6 ppm/(mg/g wet), which was used by Fischer et al. (11). To convert from wet weight to dry weight so that the estimates would be consistent with Ferriscan, we used a factor of 4.1, as measured by Zuyderhoudt et al. (49). The total LIC, expressed in mg Fe/g dry tissue, was then calculated as the sum of the baseline iron concentration and the overload iron concentration.

In addition, liver R2* was measured from the R2* map that was estimated by the chemical shift encoded reconstruction (50). The liver R2* was measured in the same location as the liver susceptibility, at both 1.5T and 3T.

Finally, the spin-echo acquisitions obtained at 1.5T were processed using Ferriscan, which is an R2-based measurement of LIC using the calibration derived by St. Pierre et al. (12). The acquired MR data were uploaded to Resonance Health (Claremont, Australia). The resulting reports, which included an estimate of LIC in mg Fe/g dry tissue, were electronically received within two business days.

Statistical Analysis

Linear regression analysis was performed to investigate the correlation between liver susceptibility and the Ferriscan-based estimate of LIC. Using the three different conversion factors mentioned earlier, the agreement between the susceptibility-based estimate of LIC and Ferriscan-LIC was analyzed. Because the baseline iron concentration was calculated from the control subjects, these comparisons were performed only in the subjects with known or suspected iron overload.

In addition, for both 1.5T and 3T, linear regression was performed to analyze the correlation between liver susceptibility and liver R2*. Finally, linear regression and Bland-Altman analyses were performed to determine the agreement between estimates of liver susceptibility at 1.5T and 3T. The comparison between liver susceptibility and liver R2* as well as the comparison between 1.5T and 3T were performed in all subjects.

RESULTS

For three subjects, significant image artifacts prevented reliable measurements of susceptibility. Severe respiratory motion was observed for one subject at 3T, a large water-fat separation error (which affected the estimated B_0 field map) occurred in another subject at 1.5T, and severe parallel imaging artifact occurred for a third subject at 3T. In these three cases, the data were excluded from all further analyses; the corresponding data acquired at the other field strength were preserved. The QSM reconstruction was successful in the remaining subjects. In a few of these remaining cases, minimal parallel imaging or water-fat separation artifacts were observed. In these cases, the analyses were performed in regions that avoided the image artifact.

Figure 4 shows the measured B_0 field map and the corresponding susceptibility map at both 1.5T and 3T for three subjects with varying levels of liver iron. The susceptibility of the

liver, measured relative to the subcutaneous adipose tissue, is also shown. As the hepatic iron overload increases, the susceptibility in the liver increases (i.e. becomes more positive). This is expected since iron is paramagnetic. For each subject, the susceptibility estimates of the liver at 1.5T and 3T are in good agreement. Notice the variations of the B_0 field maps in regions of homogeneous tissue (e.g. subcutaneous adipose tissue), which result from the nonlocal response of the dipole kernel. The variations are especially pronounced in the subject with no liver iron overload, and result from air in the gut. In contrast, in the estimated susceptibility map, uniformity of the subcutaneous adipose tissue is observed. The average standard deviation, across subjects, of the susceptibility estimates in the subcutaneous adipose tissue is 0.025 ± 0.027 ppm.

Figure 5 shows the measured B_0 field map and its decomposition into the local field and the background field components. The local field was estimated by applying the forward dipole transform to the estimated local susceptibility distribution (i.e. $\psi_L = D\chi_L$). The background field was then calculated as the difference between the measured B_0 field and the estimated local field (i.e. $\psi_B = \psi - \psi_L$). It is observed that the local field reflects information about the local susceptibility distribution, such as the edges between fat and muscle (black arrows). The background field reflects information about the background susceptibility sources, although some trace of anatomical structure (e.g. muscle-liver interface in subject #2) can be observed. It is interesting to note that components of the local field are observed in the measured B0 field. This observation suggests that the background field does not dominate the local field, unlike in the brain where the background field is the major contribution to the measured B_0 field.

Figure 6 plots the liver susceptibility versus the Ferriscan-LIC, at both 1.5T and 3T. The baseline susceptibility difference and baseline iron concentration, measured from the control subjects, was −0.31 ppm and 0.99 mg/g dry, respectively. The coefficient of determination between liver susceptibility and Ferriscan-LIC was $R^2 = 0.76$ at 1.5T and $R^2 = 0.83$ at 3T. Also shown in Figure 5 is a table of the slope and y-intercept values using the three different conversion factors. The datasets from the control subjects were not included in the linear regression analyses since they were used for the baseline measurements.

Figure 7 shows the relationship between liver susceptibility and liver R2* at both 1.5T and 3T. Also shown are the linear regression and Bland-Altman plots that analyze the liver susceptibility measurements at 1.5T and 3T. Correlation between liver susceptibility and liver R2* was $R^2 = 0.94$ at 1.5T and $R^2 = 0.93$ at 3T. Linear regression analysis of the liver susceptibility measurements at 1.5T and 3T yielded a slope = 0.96, y-intercept = −0.05 ppm, and $R^2 = 0.96$. Bland-Altman analysis showed a 95% confidence interval of [−0.29, 0.43] ppm. The mean difference in susceptibility measurements at 1.5T versus 3T was equal to 0.07 ppm, which was statistically significant (p = 0.03).

DISCUSSION

In this work, we have developed and demonstrated initial clinical validation of a quantitative susceptibility mapping technique in the abdomen as an imaging biomarker of hepatic iron overload. Estimates of liver susceptibility demonstrated good correlation with liver iron

concentration measured using Ferriscan ($R^2 = 0.76$ at 1.5T; $R^2 = 0.83$ at 3T). Recent work from Wood et al. (51) showed a similar goodness of fit ($R^2 = 0.75$) between an R2* measure of LIC and Ferriscan-LIC, while Chan et al. report $R^2 = 0.94$ between liver R2* and Ferriscan-LIC (52). The discordance between the goodness of fit observed by Chan et al. and that observed in the current study are a source of concern if susceptibility-based estimates of LIC are to be used in place of R2*-based estimates. This discordance will be studied in future works.

The liver susceptibility measurements demonstrated high correlation with liver R2* ($R^2 = 0.94$ at 1.5T; $R^2 = 0.93$ at 3T). This correlation is worth noting since these two parameters were estimated independently of one another from the same gradient echo dataset. However, their correlation is not unexpected, since R2*-based methods have demonstrated good correlation with LIC (13,14). High correlation was also observed between liver susceptibility measurements at 1.5T and 3T. The cause of the slight positive bias of 0.07 ppm at 1.5T requires further investigation.

The results from this work suggest that QSM may serve as an imaging biomarker of liver iron concentration. An advantage to quantifying susceptibility is that it is a fundamental property of materials (including iron and liver tissue), in contrast to empirical relaxation parameters (e.g. R2 and R2*), which may be confounded by other factors. Although our findings are preliminary, they demonstrate the promise for QSM to serve as an imaging biomarker of hepatic iron overload.

The calculation of LIC from susceptibility relies on conversion factors that have not yet been fully characterized. Therefore, we chose three conversion factors from the literature to compare susceptibility-based LIC to Ferriscan-LIC. In all cases, linear regression yielded a slope less than one (i.e. Ferriscan-LIC > susceptibility-based LIC). A similar trend was also found by Wood et al. (51) when comparing Ferriscan and R2* (i.e. Ferriscan-LIC > R2*-LIC). These discrepancies do not necessarily suggest a specific bias in any one of the techniques, but may instead reflect the different response of the parameters (i.e. R2, R2*, susceptibility) to the size and distribution of iron deposition (51). Further work is needed to fully characterize the susceptibility of iron within the liver.

The current study did not compare the MR-based estimates of liver susceptibility to those from BLS due to the unavailability of a SQUID susceptometer. We are aware of only four such devices worldwide that are currently in use for BLS (10,53). Comparison with BLS is needed in future studies and may provide definitive evidence about the accuracy of liver susceptibility measurements using the proposed MR-based technique.

Quantifying liver iron was the focus of this work. However, because the full dipole inversion was performed, a susceptibility map throughout the entire abdomen was estimated. The susceptibility values in other organs within the abdomen, such as the pancreas, spleen, and kidneys, could also be measured as potential imaging biomarkers of iron overload or other organ-specific disease states. All of these organs can be affected by iron overload in a variety of disease states.

The QSM reconstruction was implemented using a joint background field removal and dipole inversion formulation. This formulation permitted estimation of the local susceptibility distribution directly from the B_0 field map. A limitation of this joint approach is that the individual performance of the two components (i.e. background field removal and dipole inversion) cannot be evaluated in a straightforward manner. For example, a separate analysis would be needed to determine the cause of the residual anatomical structure that is observed in the background field of subject #2 (Fig. 5). However, the results in this work have demonstrated good correlation of liver susceptibility estimates with both liver R2* and Ferriscan-LIC.

In this work, an anatomically weighted l_2-penalty was applied to the susceptibility map to regularize the inversion. The l_2-penalty has been shown to provide sufficient regularization for applications in brain QSM (32). Further, unlike the l_1-penalty, the reconstruction problem may still be formulated as a linear inversion and solved using linear conjugate gradients. More recent work has explored the use of the l_1-penalty in brain QSM under the compressed sensing framework (16,54), although no significant difference was found between the two methods (36). A comparison between these two regularization penalties has not yet been performed for liver QSM.

The data for this study were acquired using the six-echo chemical shift encoded acquisition that is used at our institution for water-fat separation and quantification. As such, the acquisition parameters were chosen to ensure reliable estimates of water and fat (55,56), rather than with regard to the quality of the B_0 field map estimate. For QSM, however, the B_0 field map is the primary parameter of interest from the chemical shift encoded reconstruction. Thus, it may be possible to optimize the acquisition parameters for the estimate of the B_0 field map, which in turn, may lead to more reliable estimates of the susceptibility map. Determining the optimal acquisition parameters for B_0 field map estimation remains to be performed in the future.

In conclusion, we have successfully developed and demonstrated feasibility and initial clinical validation of a new approach for abdominal QSM aimed at quantifying hepatic iron overload. Liver susceptibility estimates demonstrated good correlation with both Ferriscan-LIC and liver R2*. The proposed technique shows promise as an imaging biomarker of hepatic iron overload that is based on a fundamental property of materials.

ACKNOWLEDGEMENTS

REFERENCES

1. Gordeuk VR, Bacon BR, Brittenham GM. Iron overload: causes and consequences. Annual review of nutrition. 1987; 7(1):485–508.

2. Olivieri NF, Brittenham GM. Iron-chelating therapy and the treatment of thalassemia. Blood. 1997; 89(3):739–761. [PubMed: 9028304]

3. Frazer DM, Anderson GJ. Iron imports. I. Intestinal iron absorption and its regulation. American Journal of Physiology-Gastrointestinal and Liver Physiology. 2005; 289(4):G631–G635. [PubMed: 16160078]

4. Porter JB. Practical management of iron overload. British journal of haematology. 2001; 115(2): 239–252. [PubMed: 11703317]

5. Vichinsky E. Oral iron chelators and the treatment of iron overload in pediatric patients with chronic anemia. Pediatrics. 2008; 121(6):1253–1256. [PubMed: 18519495]

6. Nielsen P, Günther U, Dürken M, Fischer R, Düllmann J. Serum ferritin iron in iron overload and liver damage: correlation to body iron stores and diagnostic relevance. Journal of Laboratory and Clinical Medicine. 2000; 135(5):413–418. [PubMed: 10811057]

7. Brittenham GM, Badman DG. Noninvasive measurement of iron: report of an NIDDK workshop. Blood. 2003; 101(1):15–19. [PubMed: 12393526]

8. Ratziu V, Charlotte F, Heurtier A, Gombert S, Giral P, Bruckert E, Grimaldi A, Capron F, Poynard T. Sampling variability of liver biopsy in nonalcoholic fatty liver disease. Gastroenterology. 2005; 128(7):1898–1906. [PubMed: 15940625]

9. Bauman JH, Harris JW. Estimation of hepatic iron stores by vivo measurement of magnetic susceptibility. The Journal of laboratory and clinical medicine. 1967; 70(2):246. [PubMed: 6029057]

10. Nielsen P, Engelhardt R, Duerken M, Janka G, Fischer R. Using SQUID biomagnetic liver susceptometry in the treatment of thalassemia and other iron loading diseases. Transfusion science. 2000; 23(3):257–258. [PubMed: 11099909]

11. Fischer R, Piga A, Harmatz P, NIelsen P. Monitoring Long-Term Efficacy of Iron Chelation Treatment with Biomagnetic Liver Susceptometry. Annals of the New York Academy of Sciences. 2005; 1054(1):350–357. [PubMed: 16339683]

12. St Pierre TG, Clark PR, Chua-anusorn W. Single spin-echo proton transverse relaxometry of iron-loaded liver. NMR in Biomedicine. 2004; 17(7):446–458. [PubMed: 15523601]

13. Wood JC, Enriquez C, Ghugre N, Tyzka JM, Carson S, Nelson MD, Coates TD. MRI R2 and R2* mapping accurately estimates hepatic iron concentration in transfusion-dependent thalassemia and sickle cell disease patients. Blood. 2005; 106(4):1460–1465. [PubMed: 15860670]

14. Hankins JS, McCarville MB, Loeffler RB, Smeltzer MP, Onciu M, Hoffer FA, Li C-S, Wang WC, Ware RE, Hillenbrand CM. R2* magnetic resonance imaging of the liver in patients with iron overload. Blood. 2009; 113(20):4853–4855. [PubMed: 19264677]

15. Wharton S, Schäfer A, Bowtell R. Susceptibility mapping in the human brain using threshold-based k-space division. Magnetic Resonance in Medicine. 2010; 63(5):1292–1304. [PubMed: 20432300]

16. Liu T, Liu J, de Rochefort L, Spincemaille P, Khalidov I, Ledoux JR, Wang Y. Morphology enabled dipole inversion (MEDI) from a single-angle acquisition: Comparison with COSMOS in human brain imaging. Magnetic resonance in medicine. 2011; 66(3):777–783. [PubMed: 21465541]

17. Schweser F, Deistung A, Lehr BW, Reichenbach JR. Quantitative imaging of intrinsic magnetic tissue properties using MRI signal phase: an approach to in vivo brain iron metabolism? Neuroimage. 2011; 54(4):2789–2807. [PubMed: 21040794]

18. Wang ZJ, Li S, Haselgrove JC. Magnetic resonance imaging measurement of volume magnetic susceptibility using a boundary condition. Journal of Magnetic Resonance. 1999; 140(2):477–481. [PubMed: 10497053]

19. Chu Z, Cohen AR, Muthupillai R, Chung T, Wang ZJ. MRI measurement of hepatic magnetic susceptibility—Phantom validation and normal subject studies. Magnetic resonance in medicine. 2004; 52(6):1318–1327. [PubMed: 15562494]

20. Hernando D, Cook RJ, Diamond C, Reeder SB. Magnetic susceptibility as a B0 field strength independent MRI biomarker of liver iron overload. Magn Reson Med. 2013; 70(3):648–656. [PubMed: 23801540]

21. Liu T, Khalidov I, de Rochefort L, Spincemaille P, Liu J, Tsiouris AJ, Wang Y. A novel background field removal method for MRI using projection onto dipole fields (PDF). NMR in Biomedicine. 2011; 24(9):1129–1136. [PubMed: 21387445]

22. Salomir R, de Senneville BD, Moonen CTW. A fast calculation method for magnetic field inhomogeneity due to an arbitrary distribution of bulk susceptibility. Concepts in Magnetic Resonance Part B: Magnetic Resonance Engineering. 2003; 19B(1):26–34.

23. Marques JP, Bowtell R. Application of a Fourier-based method for rapid calculation of field inhomogeneity due to spatial variation of magnetic susceptibility. Concepts in Magnetic Resonance Part B: Magnetic Resonance Engineering. 2005; 25B(1):65–78.

24. Koch KM, Papademetris X, Rothman DL, de Graaf RA. Rapid calculations of susceptibility-induced magnetostatic field perturbations for in vivo magnetic resonance. Phys Med Biol. 2006; 51(24):6381–6402. [PubMed: 17148824]

25. de Rochefort L, Brown R, Prince MR, Wang Y. Quantitative MR susceptibility mapping using piece-wise constant regularized inversion of the magnetic field. Magnetic Resonance in Medicine. 2008; 60(4):1003–1009. [PubMed: 18816834]

26. Gudbjartsson H, Patz S. The Rician distribution of noisy MRI data. Magnetic Resonance in Medicine. 1995; 34(6):910–914. [PubMed: 8598820]

27. Li L, Leigh JS. High-precision mapping of the magnetic field utilizing the harmonic function mean value property. Journal of magnetic resonance. 2001; 148(2):442–448. [PubMed: 11237651]

28. Sun H, Wilman AH. Background field removal using spherical mean value filtering and Tikhonov regularization. Magnetic Resonance in Medicine. 2014; 71:1151–1157. [PubMed: 23666788]

29. Andrew E, Bradbury A, Eades R. Nuclear magnetic resonance spectra from a crystal rotated at high speed. Nature. 1958; 182:1659.

30. Shmueli K, de Zwart JA, van Gelderen P, Li TQ, Dodd SJ, Duyn JH. Magnetic susceptibility mapping of brain tissue in vivo using MRI phase data. Magnetic Resonance in Medicine. 2009; 62(6):1510–1522. [PubMed: 19859937]

31. Haacke E, Tang J, Neelavalli J, Cheng Y. Susceptibility mapping as a means to visualize veins and quantify oxygen saturation. Journal of Magnetic Resonance Imaging. 2010; 32(3):663–676. [PubMed: 20815065]

32. de Rochefort L, Liu T, Kressler B, Liu J, Spincemaille P, Lebon V, Wu J, Wang Y. Quantitative susceptibility map reconstruction from MR phase data using bayesian regularization: validation and application to brain imaging. Magnetic Resonance in Medicine. 2010; 63(1):194–206. [PubMed: 19953507]

33. Liu T, Spincemaille P, de Rochefort L, Kressler B, Wang Y. Calculation of susceptibility through multiple orientation sampling (COSMOS): a method for conditioning the inverse problem from measured magnetic field map to susceptibility source image in MRI. Magnetic Resonance in Medicine. 2009; 61(1):196–204. [PubMed: 19097205]

34. Szczepaniak LS, Nurenberg P, Leonard D, Browning JD, Reingold JS, Grundy S, Hobbs HH, Dobbins RL. Magnetic resonance spectroscopy to measure hepatic triglyceride content: prevalence of hepatic steatosis in the general population. American Journal of Physiology-Endocrinology and Metabolism. 2005; 288(2):E462–E468. [PubMed: 15339742]

35. Langkammer C, Schweser F, Krebs N, Deistung A, Goessler W, Scheurer E, Sommer K, Reishofer G, Yen K, Fazekas F. Quantitative susceptibility mapping (QSM) as a means to measure brain iron? A post mortem validation study. Neuroimage. 2012; 62(3):1593–1599. [PubMed: 22634862]

36. Bilgic B, Pfefferbaum A, Rohlfing T, Sullivan EV, Adalsteinsson E. MRI estimates of brain iron concentration in normal aging using quantitative susceptibility mapping. Neuroimage. 2012; 59(3): 2625–2635. [PubMed: 21925274]

37. Reeder SB, Pineda AR, Wen Z, Shimakawa A, Yu H, Brittain JH, Gold GE, Beaulieu CH, Pelc NJ. Iterative decomposition of water and fat with echo asymmetry and least-squares estimation (IDEAL): application with fast spin-echo imaging. Magn Reson Med. 2005; 54(3):636–644. [PubMed: 16092103]

38. Hernando D, Kellman P, Haldar J, Liang ZP. Robust water/fat separation in the presence of large field inhomogeneities using a graph cut algorithm. Magnetic Resonance in Medicine. 2010; 63(1): 79–90. [PubMed: 19859956]

39. Yu H, Shimakawa A, McKenzie CA, Brodsky E, Brittain JH, Reeder SB. Multiecho water-fat separation and simultaneous R 2* estimation with multifrequency fat spectrum modeling. Magnetic Resonance in Medicine. 2008; 60(5):1122–1134. [PubMed: 18956464]

40. Hamilton G, Yokoo T, Bydder M, Cruite I, Schroeder ME, Sirlin CB, Middleton MS. In vivo characterization of the liver fat 1H MR spectrum. NMR in biomedicine. 2011; 24(7):784–790. [PubMed: 21834002]

41. Knutson M, Wessling-Resnick M. Iron metabolism in the reticuloendothelial system. Critical reviews in biochemistry and molecular biology. 2003; 38(1):61–88. [PubMed: 12641343]

42. Boyd, SP.; Vandenberghe, L. Convex optimization. Cambridge university press; 2004.

43. Liu CY, McKenzie CA, Yu H, Brittain JH, Reeder SB. Fat quantification with IDEAL gradient echo imaging: correction of bias from T1 and noise. Magnetic Resonance in Medicine. 2007; 58(2):354–364. [PubMed: 17654578]

44. Hestenes MR, Stiefel E. Methods of conjugate gradients for solving linear systems. Journal of Research National Bureau of Standards. 1952; 49:409–436.

45. Schweser F, Sommer K, Atterbury M, Deistung A, Lehr B, Reichenbach J. On the impact of regularization and kernel type on SHARP-corrected GRE phase images. 2011:2667.

46. Porat, B. A course in digital signal processing. New York: Wiley; 1997.

47. Hansen PC. Analysis of discrete ill-posed problems by means of the L-curve. SIAM review. 1992; 34(4):561–580.

48. Ghugre NR, Wood JC. Relaxivity-iron calibration in hepatic iron overload: Probing underlying biophysical mechanisms using a Monte Carlo model. Magnetic Resonance in Medicine. 2011; 65(3):837–847. [PubMed: 21337413]

49. Zuyderhoudt F, Hengeveld P, Van Gool J, Jörning G. A method for measurement of liver iron fractions in needle biopsy specimens and some results in acute liver disease. Clinica Chimica Acta. 1978; 86(3):313–321.

50. Hernando D, Kramer JH, Reeder SB. Multipeak fat-corrected complex R2* relaxometry: Theory, optimization, and clinical validation. Magnetic Resonance in Medicine. 2013; 70(5):1319–1331. [PubMed: 23359327]

51. Wood JC, Zhang P, Rienhoff H, Abi-Saab W, Neufeld E. R2 and R2* are equally effective in evaluating chronic response to iron chelation. American journal of hematology. 2014; 89(5):505–508. [PubMed: 24452753]

52. Chan WC, Tejani Z, Budhani F, Massey C, Haider MA. R2* as a surrogate measure of ferriscan iron quantification in thalassemia. Journal of Magnetic Resonance Imaging. 2014; 39(4):1007–1011. [PubMed: 24123694]

53. Paulson D, Fagaly R, Toussaint R, Fischer R. Biomagnetic susceptometer with SQUID instrumentation. Magnetics, IEEE Transactions on. 1991; 27(2):3249–3252.

54. Wu B, Li W, Guidon A, Liu C. Whole brain susceptibility mapping using compressed sensing. Magnetic Resonance in Medicine. 2012; 67(1):137–147. [PubMed: 21671269]

55. Pineda AR, Reeder SB, Wen Z, Pelc NJ. Cramer-Rao bounds for three-point decomposition of water and fat. Magn Reson Med. 2005; 54(3):625–635. [PubMed: 16092102]

56. Reeder SB, Bice EK, Yu H, Hernando D, Pineda AR. On the performance of T2* correction methods for quantification of hepatic fat content. Magnetic Resonance in Medicine. 2012; 67(2):389–404. [PubMed: 21661045]
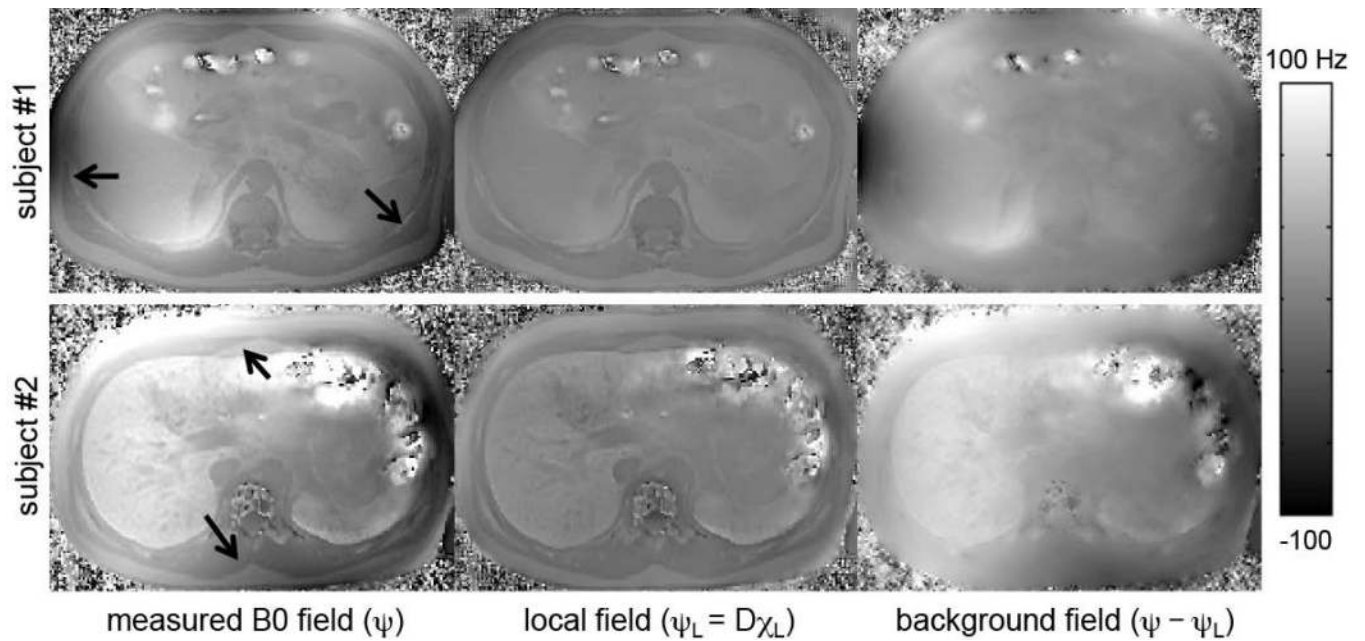
Figure 1.
Processing pipeline to estimate the susceptibility maps in the abdomen. Complex source images (magnitude shown) are acquired using a six-echo gradient-echo acquisition. A chemical shift encoded reconstruction is used to estimate the B_0 field map, as well as the R2* map and the separated water and fat images (magnitude images shown). A fat mask is derived from the separated water and fat images. The edge weighting and data weighting masks are derived from the source images. The susceptibility map is then estimated using the proposed background field removal and dipole inversion technique. Finally, the liver iron concentration is calculated from the susceptibility map.
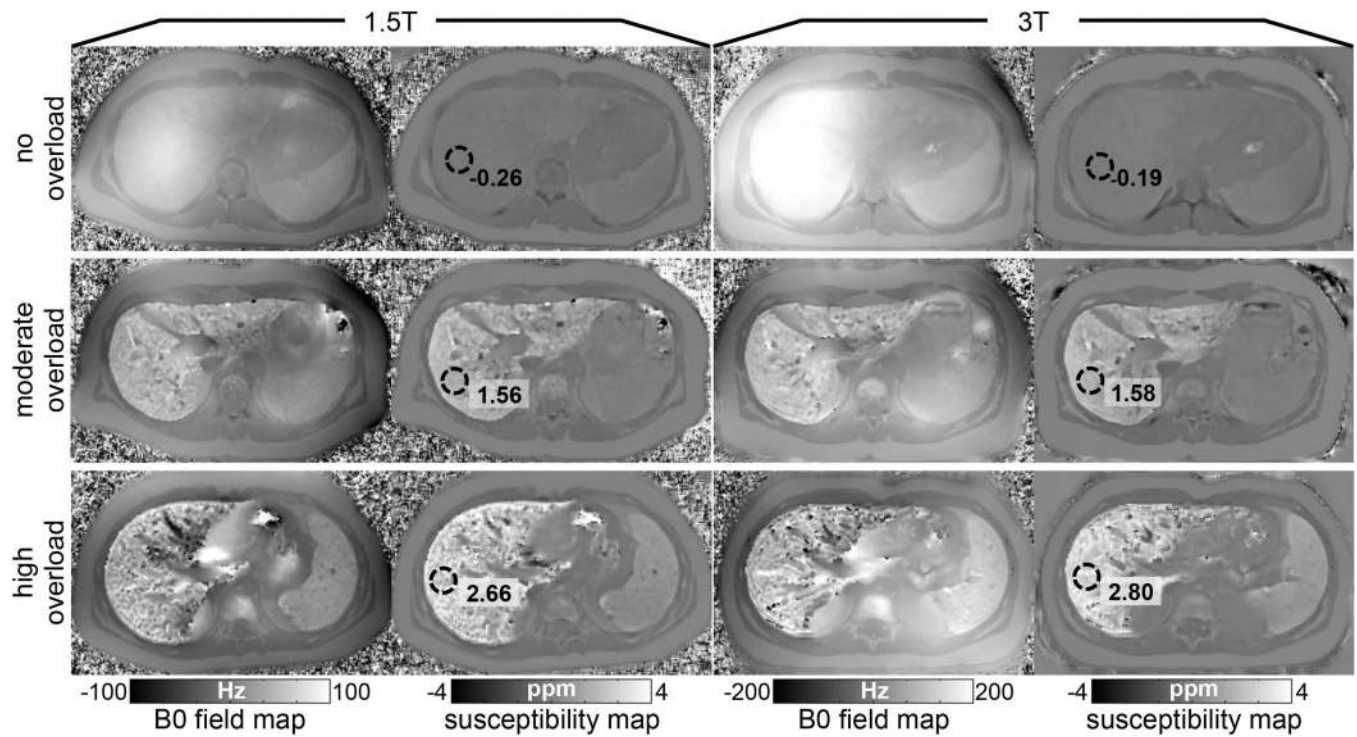
Figure 2.
The edge weighting is calculated based on the tissue boundaries that reflect either chemical shift contrast or R2* contrast. Because edge locations are not penalized in the susceptibility map, they appear as dark regions (i.e. low value) in the weighting image. An edge that appears in either the chemical shift contrast weighting or the R2* contrast weighting will appear in the composite weighting. The arrows indicate edges that appear in either the chemical shift or R2* contrast weighting, but not both. The fat constraint acts to further suppress variations in the adipose tissue, which does not accumulate excess iron and is assumed to have uniform susceptibility.
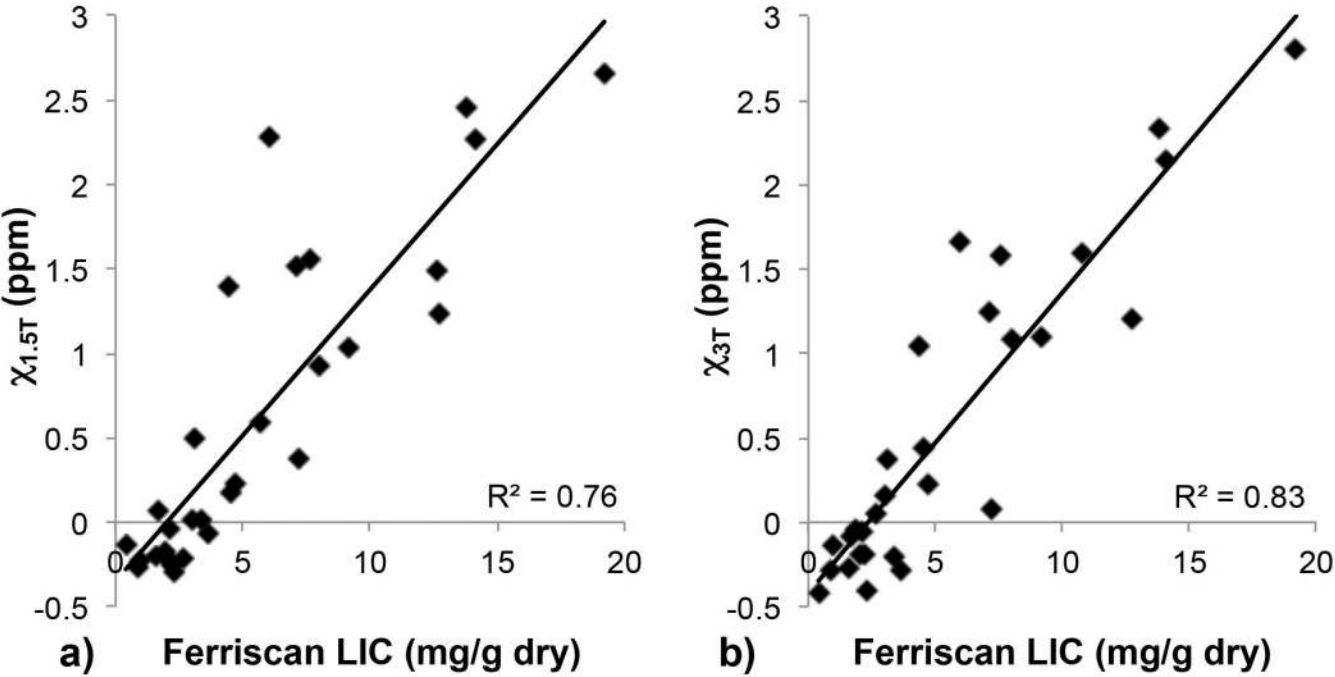
	conversion factor	slope (1.5T)	intercept (1.5T)	slope (3T)	intercept (3T)
Langkammer [35]	0.217	0.79 [0.62, 0.97]	0.82 [-0.45, 2.1]	0.82 [0.68, 0.97]	0.49 [-0.56, 1.54]
Ghugre [48]	0.293	0.59 [0.46, 0.72]	0.86 [-0.08, 1.81]	0.61 [0.5, 0.71]	0.62 [-0.16, 1.4]
Fischer [11]	0.39	0.44 [0.34, 0.54]	0.89 [0.19, 1.6]	0.46 [0.38, 0.54]	0.71 [0.13, 1.3]

Figure 3.
The L-curve analysis demonstrates the tradeoff between data fidelity and regularization as a function of the regularization parameter λ. The regularization norm and the residual norm were calculated using the entire imaging volume. A low λ value results in artifacts from the ill-posed nature of the inverse problem whereas a high λ value causes over-regularization. Using these results together with visual inspection of the estimated susceptibility maps, a regularization parameter of $\lambda = 2 \times 10^{-1}$ was chosen for all reconstructions presented here.
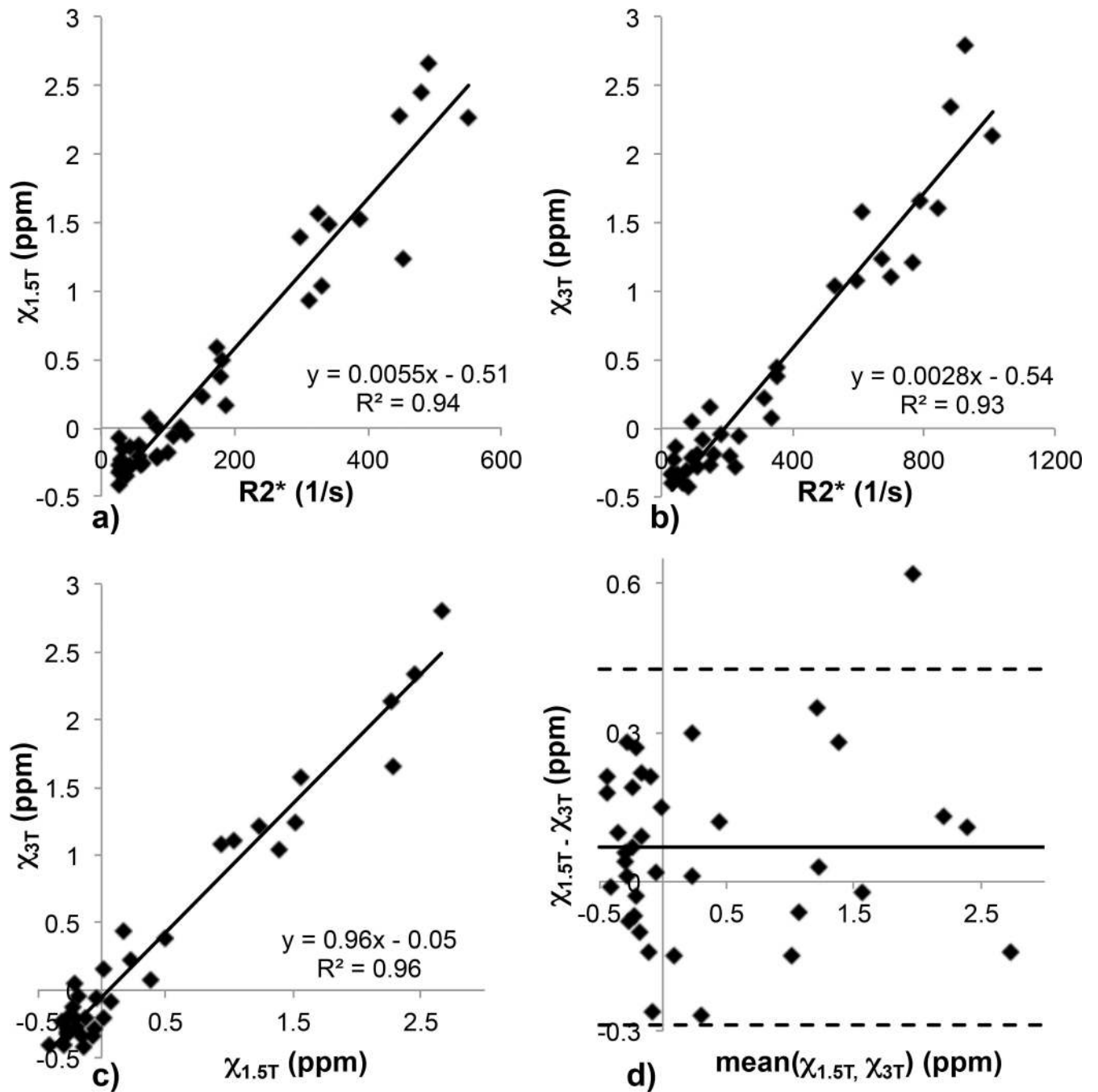
Figure 4.
B_0 field maps and the corresponding susceptibility maps at 1.5T and 3T for three subjects with different levels of iron overload. The susceptibility value measured in the ROI is relative to the subcutaneous adipose tissue. As expected, liver susceptibility increases with increasing iron overload. Good agreement is seen between susceptibility measured at 1.5T and 3T for each subject.
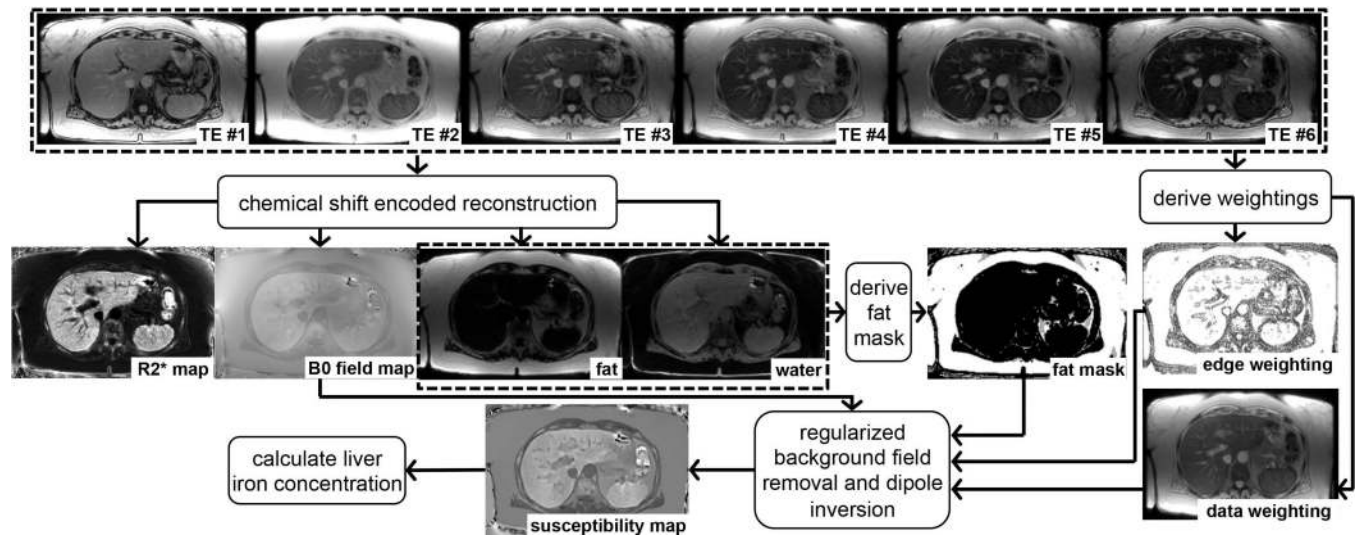
Figure 5.

The measured B_0 field can be decomposed into the local field and background field components. The black arrows highlight regions of fat-muscle interfaces, which are correctly reflected in the local field but not the background field.
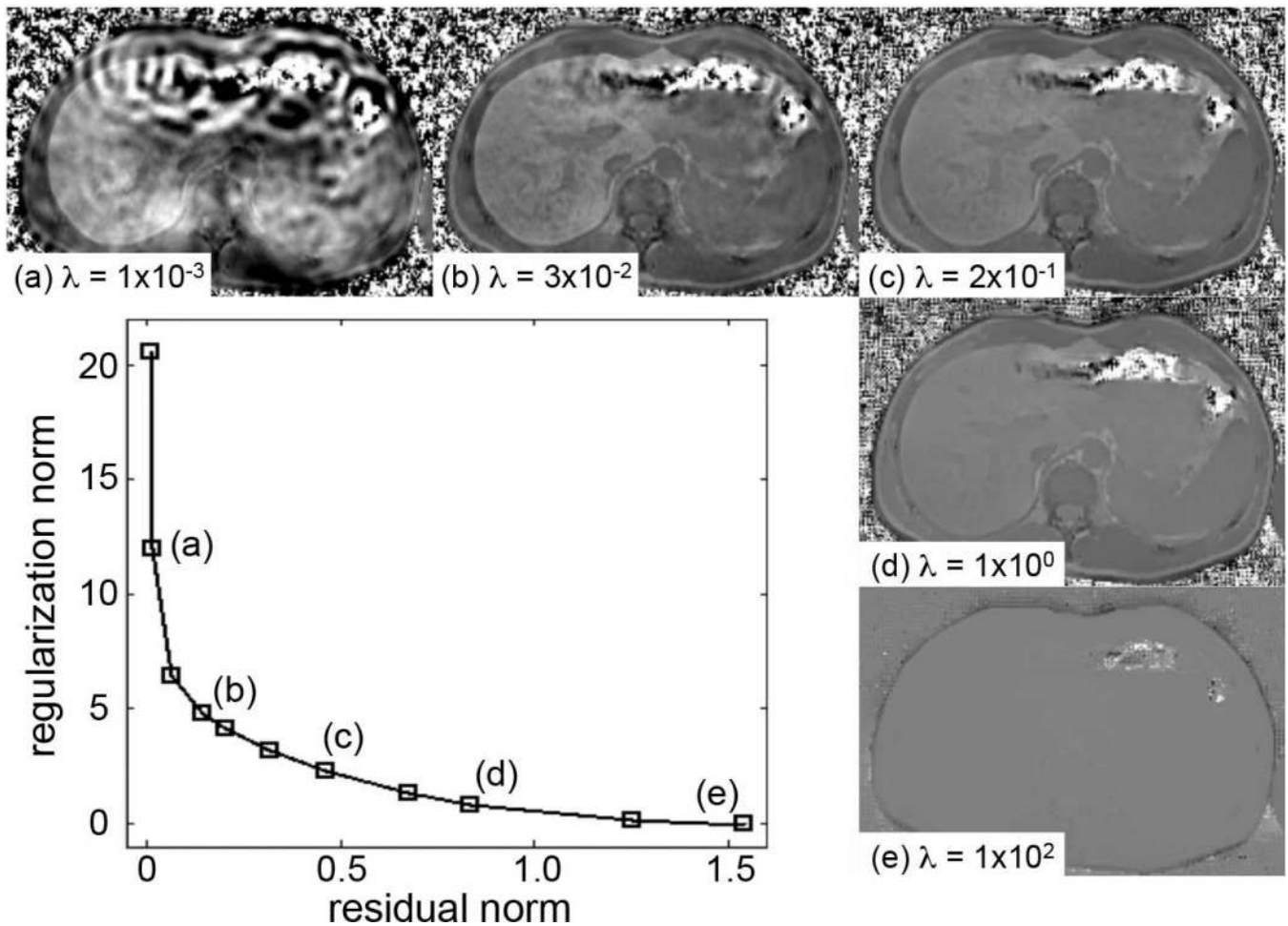
Figure 6.
Liver susceptibility versus Ferriscan-based estimates of LIC at 1.5T (a) and 3T (b). The coefficient of determination between susceptibility and Ferriscan-LIC was $R^2 = 0.76$ at 1.5T and $R^2 = 0.83$ at 3T. The table shows the slope and y-intercept values using three different conversion factors from susceptibility to LIC (mg/g dry). The 95% confidence intervals are shown in brackets. Note that the conversion factors shown in the table assume a wet weight to dry weight conversion factor of 4.1. The datasets from the control subjects were not included in the linear regression analyses since they were used for the baseline measurements.
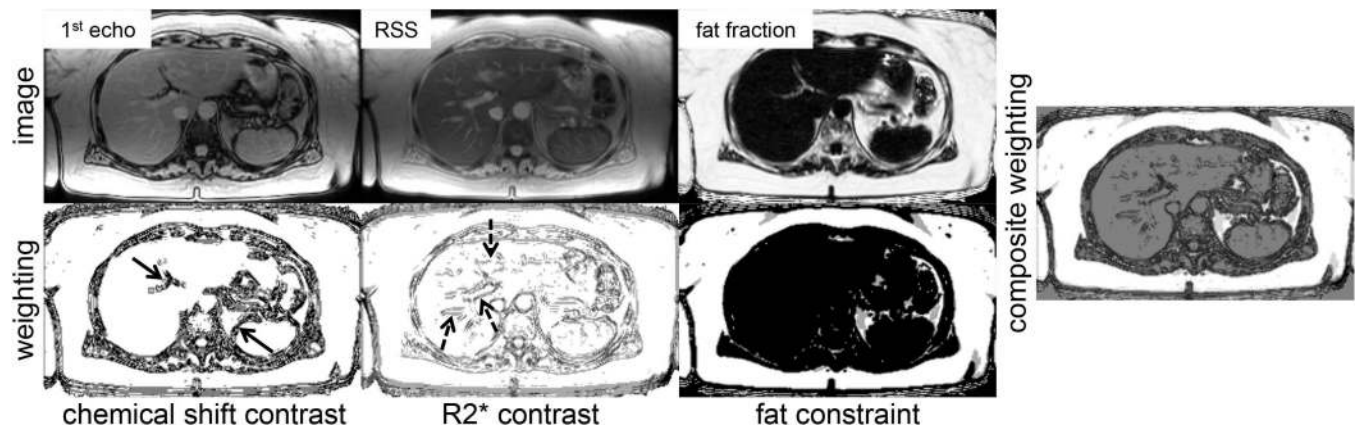
Figure 7.
High correlation was observed between liver susceptibility and liver R2*, at both 1.5T (a) and 3T (b). Agreement and correlation between susceptibility measurements at 1.5T and 3T were characterized by the following parameters: slope = 0.96, y-intercept = −0.05 ppm, and R^2 = 0.96 (c). Bland-Altman analysis of liver susceptibility measurements at 1.5T and 3T indicated a 95% confidence interval equal to [−0.29, 0.43] ppm (d).

Table 1

Acquisition parameters for the datasets in this study. nTE denotes the number of echoes, ETL is the echo train length, RBW is the receiver bandwidth, and PI represents the parallel imaging acceleration (phase encode × slice encode). All data were acquired in the axial imaging plane.

Sequence	Field Strength (T)	TE1 (ms)	ΔTE (ms)	nTE	ETL	TR (ms)	Scan time	Flip angle (deg.)	RBW (kHz)	PI	FOV (cm)	Acquired resolution (mm)	Acquired matrix size
3D gradient-echo	1.5	1.2	2	6	6	14	19s	5	±125	2 × 2	40 × 36	1.6 × 2.3 × 8	256 × 160 × 32
3D gradient-echo	3	1.2	1	6	3	8.6	22s	3	±125	2 × 2	40 × 32	1.6 × 2.2 × 8	256 × 144 × 32
2D spin-echo	1.5	6	3	5	1	1000	18m	90	±62.5	1 × 1	44 × 44	1.7 × 1.7 × 6	256 × 256 × 11